The Glassy Structure Formation and Phase Evolution in Mechanically Alloyed and Spark Plasma-Sintered Al-TM-RE Alloys

Ram S. Maurya and **Tapas Laha**

The present study deals with the comparative study of amorphization tendency of $Al_{86}Ni_6Y_6$, $Al_{86}Ni_6Y_6Co_2$ and $Al_{86}Ni_6Y_{4.5}Co_2La_{1.5}$ alloy powders via mechanical alloying performed at 300 revolution per minute with ball-to-powder ratio of 15:1 and subsequently the devitrification tendency of 300 °C and 500 °C spark plasma-sintered bulk amorphous alloys. Mechanically alloyed $Al_{86}Ni_6Y_6$, $Al_{86}Ni_6Y_6Co_2$ and $Al_{86}Ni_6Y_{4.5}Co_2La_{1.5}$ powders yielded nearly fully amorphous structure after 140, 170 and 200 h, respectively. The requirement of prolonged milling was attributed to the soft and ductile nature of aluminum with high stacking fault energy. Amorphous powders were consolidated via spark plasma sintering at 300 and 500 °C by applying a constant pressure of 500 MPa. X-ray diffraction was performed on the 300- and 500 °C-sintered samples. XRD patterns of the 300 °C-sintered alloys exhibited very-low-intensity nanocrystalline FCC-Al peak overlaying an amorphous hump evincing retention of a large amount of the amorphous phase. Enhanced devitrification tendency was reported in the 500 °C-sintered alloys; however, a major difference in the devitrification tendency of the 500 °C-sintered $Al_{86}Ni_8Y_6$, $Al_{86}Ni_6Y_6Co_2$ and $Al_{86}Ni_6Y_{4.5}Co_2La_{1.5}$ alloys was that the quinary alloy exhibited higher tendency of devitrification, which was also corroborated by performing HRTEM and analytical TEM experiment. This could be attributed to the higher probability of coupling of atoms by short-range atomic shuffling during spark plasma sintering. Vickers hardness, and relative density estimated via Archimedes' principle, varied depending on the degree of free volume annihilation and crystallization during sintering.

1. Introduction

Bulk metallic glasses (BMGs), having outstanding mechanical, chemical and physical properties, could replace the presently used metallic materials in many structural and functional applications (Ref [1], [2]). Aluminum-based BMGs possess lower density along with high specific strength and thus can be extensively used in aerospace industry (Ref [1]-[4]). The particular combination of Al ($\geq$ 80%)-TM (Ni, Co, Fe)-RE (Y, La, Ce) has been predicted as good glass former based on the efficient cluster packing model which ensures reduction in thermodynamic free volumes and lower system energy (Ref [5], [6]). Unfortunately, the major hurdle in fabricating Al-rich glassy alloys is the requirement of high quenching rate attributed to the low glass transition temperature as Al-rich amorphous compositions are located largely away from their eutectic points where the liquidus temperature rises steeply and thus posses low glass transition temperature range (Ref [7]). This limits the thickness of Al-rich glassy alloys and restricts their engineering application.

However, the powder technology route, viz. mechanical alloying, and consecutive spark plasma sintering have stimulated a considerable progress in enhancing the various properties of Al-based glassy alloys (Ref [8]-[13]). Mechanical alloying offers bulk amount of powder synthesis with a large composition range without much restriction of phase diagram (Ref [14]). The main challenge is to sinter the amorphous powders with full densification and that too without significant devitrification. Thus, devitrification phenomena during the consolidation of amorphous powders become a necessary study for better selection of multicomponent alloys. The devitrification behavior of glassy alloys synthesized via powder metallurgy is reported to be dependent on the type and atomic size of the elements present in the alloy (Ref [15]-[20]), sintering pressure (Ref [9], [21], [22]), temperature (Ref [10], [12]) as well as time (Ref [23]). In this context, Huang et al. (Ref [15]) reported the dependence of crystallization behavior of Al-Ni-La amorphous alloys on Ni and La contents, fabricated via melt spinning. They found that La, in comparison with Ni, played a more significant role in improving glass-forming ability and thermal stability, stabilizing the supercooled region and suppressing the formation of FCC-Al phase. Similarly, Guo et al. (Ref [19]) evaluated the atomic size effect of alkali metals on quenched $Al_{87}Ni_7Gd_{6-x}(Ca, Sr, Ba)_x$ amorphous alloys. The glass-forming ability decreased with the increasing content of alkali elements at the expense of Gd.

Despite so many works on the crystallization behavior of Al-based glassy alloys (Ref [9]-[12], [21], [22]), a systematic study on the glassy structure formation and phase evolution in mechan-

Ram S. Maurya, Discipline of Metallurgy Engineering and Materials Science, Indian Institute of Technology Indore, Indore 453552, India; and **Tapas Laha**, Department of Metallurgical and Materials Engineering, Indian Institute of Technology Kharagpur, Kharagpur 721302, India. Contact e-mail: ramsajeevan@iiti.ac.in.

ically alloyed and spark plasma-sintered Al-TM (transition metal)-RE (rare earth metal) alloys is yet to be investigated. Various works have been performed to study the effect of spark plasma sintering (SPS) parameter on consolidation kinetics; however, they were not comparative in nature (Ref 9-13, 21-23). Li et al. (Ref 23) reported evolution of multiple peaks of nanometric phases in the 250 °C-sintered $Al_{86}Ni_6Y_{4.5}Co_2La_{1.5}$ amorphous alloy, whereas Sasaki et al. (Ref 13) found evolution of only FCC-Al phase in similar temperature SPSed $Al_{85}Ni_{10}La_5$ glassy alloy. Similarly, Mula et al. (Ref 24) observed evolution of multiple peaks overlaying an amorphous hump in the XRD pattern of the 500 °C SPSed $Al_{88}Ni_6Ti_6$ glassy alloys. Deng et al. (Ref 12) reported appearance of multiple XRD peaks without retention of amorphous hump in similar temperature SPSed AlNiYCoLa powders. Thus, a comparative study of various Al-based glassy alloys becomes a necessary requirement to investigate the systematic crystallization behavior.

In this study, a comparative study on the devitrification tendency of spark plasma-sintered ternary $Al_{86}Ni_8Y_6$, quaternary $Al_{86}Ni_6Y_6Co_2$ and quinary $Al_{86}Ni_6Y_{4.5}Co_2La_{1.5}$ from mechanically alloyed amorphous powders has been performed. Besides, the effect of various alloying elements on amorphization tendency of the mechanically alloyed various Al-rich powders has also been compared.

2. Experimental: Materials Synthesis and Characterization

2.1 Synthesis of Amorphous Powders Via Mechanical Milling

Powders with nominal compositions of $Al_{86}Ni_8Y_6$, $Al_{86}Ni_6Y_6Co_2$ and $Al_{86}Ni_6Y_{4.5}Co_2La_{1.5}$ (in atom %) were prepared by blending elemental powders of Al (99.5%, − 44 mesh), Ni (99.996%, − 125 mesh), Co (99.5%, − 44 mesh), Y (99.9%, − 420 mesh) and La (99.9%, − 44 mesh), procured from Alfa Aesar, MA, USA.

Mechanical alloying was performed in a RETSCH planetary ball mill (PM 200, Retsch GmbH, Germany) inside hardened steel vials using hardened steel balls of 10 mm diameter. Disk rotational speed (RPM) and ball-to-powder-weight ratio (BPR) were 300 and 15:1, respectively. One-third of the vial volume was filled with process controlling agent (PCA, Toluene) to restrict the agglomeration and powder oxidation. Steric acid (0.08 wt.%) was added to stabilize the excessive cold welding among the starting ductile powders. Mechanically alloyed $Al_{86}Ni_8Y_6$, $Al_{86}Ni_6Y_6Co_2$ and $Al_{86}Ni_6Y_{4.5}Co_2La_{1.5}$ powders yielded nearly fully amorphous structure after 140, 170 and 200 h of milling, respectively. The amorphization of the powders is reported in "Results and discussion" section. Powders were stored and SPS die filling was carried out inside a glove box under Ar atmosphere (O_2 and H_2O < 5 ppm) to avoid air contamination.

The amorphous powders were consolidated via spark plasma sintering (FUJI SPS 625, Fuji Electronic Industrial Co. Ltd., Japan). Powders were filled in tungsten carbide die-punch set of 10 mm inner diameter and placed in the SPS chamber between the graphite and tungsten carbide spacers. Sintering was carried out at 300 and 500 °C, keeping sintering pressure 500 MPa, ramping rate 100 °C/min and holding time 15 min.

The TEM samples of powder were prepared by dropping the uniform solution mixture of powder and acetone, on a copper grid. TEM samples of bulk alloys were prepared using conventional method of metallographic polishing followed by ion milling (Precision Ion Polishing System 691, Gatan, Inc., CA, USA). XRD (Bruker D8 Advance diffractometer, Germany) was performed with CuKα (λ = 1.54 Å) radiation in the 2θ range of 20°-100° to investigate the microstructural phase evolution in mechanically alloyed powders and sintered samples. HRTEM (JEM-2100 LaB$_6$, 200 kV, JEOL Inc., USA) and analytical TEM (Tecnai G2 20S-TWIN, 200 kV, FEI, USA) were employed for the confirmation of phase evolution in the mechanically alloyed powders and sintered bulk alloys.

Relative density of the samples was measured using Archimedes' setup, whereas the theoretical density was estimated using rule of mixture. The effect of microstructural morphology and various phase evolution on mechanical properties of the SPS-consolidated samples was studied by carrying out microhardness test (UHL VMHT-001, Walter Uhl, Germany) at the load of 300 gf with a dwell time of 20 s. At least five indentations were performed at four different regions of the samples, and the average of hardness value has been presented.

3. Results and Discussion

3.1 Phase Analysis of the Al-TM (Ni, Co)-RE (Y, La)-Milled Powders

3.1.1 Comparative Phase Analysis Via XRD Technique. Figure 1 shows the XRD patterns of the mechanically alloyed $Al_{86}Ni_8Y_6$, $Al_{86}Ni_6Y_6Co_2$ and $Al_{86}Ni_6Y_{4.5}Co_2La_{1.5}$ powders, where the XRD peaks broadened with progress in milling time. In comparison with 1-h milled $Al_{86}Ni_8Y_6$ powder, 20-h milled $Al_{86}Ni_8Y_6$ powder exhibits a severe peak broadening as shown in Fig. 1(a). Beyond 20 h of milling, XRD peak broadening (Fig. 1a) slowed down attributed to the difficulties in generating any more microstructural defects (viz. dislocation, anti-phase grain boundary, vacancy, stacking fault and grain refinement) in the strain-hardened particles. Refinement of internal structure such as crystallite size, lattice microstrain, and inter-particle lamellar spacing is logarithmic with milling time (Ref 8). Thus, a lower decrease in peak intensity was noticed at longer-duration milled powders than the 20-h milled ones, as revealed in Fig. 1(a). Microstructural deformation proceeded in a similar way for the other two composition powders ($Al_{86}Ni_6Y_6Co_2$ and $Al_{86}Ni_6Y_{4.5}Co_2La_{1.5}$) as well, as shown in Fig. 1(b) and (c). These two alloy powders needed to be milled up to 50 h to achieve similar peak broadening as observed in the case of 20-h milled $Al_{86}Ni_8Y_6$ powders, suggesting delayed amorphization in the quaternary and quinary alloy powders. With progressive milling, the solute elements (Ni, Co, Y and La) were dissolved in the solvent element Al (1.432 Å). According to Hume-Rothery rule, solute elements having lower atomic radii would dissolve earlier (Ref 25). Accordingly, the transition elements Ni (1.246 Å) and Co (1.253 Å) were dissolved earlier in comparison with the rare
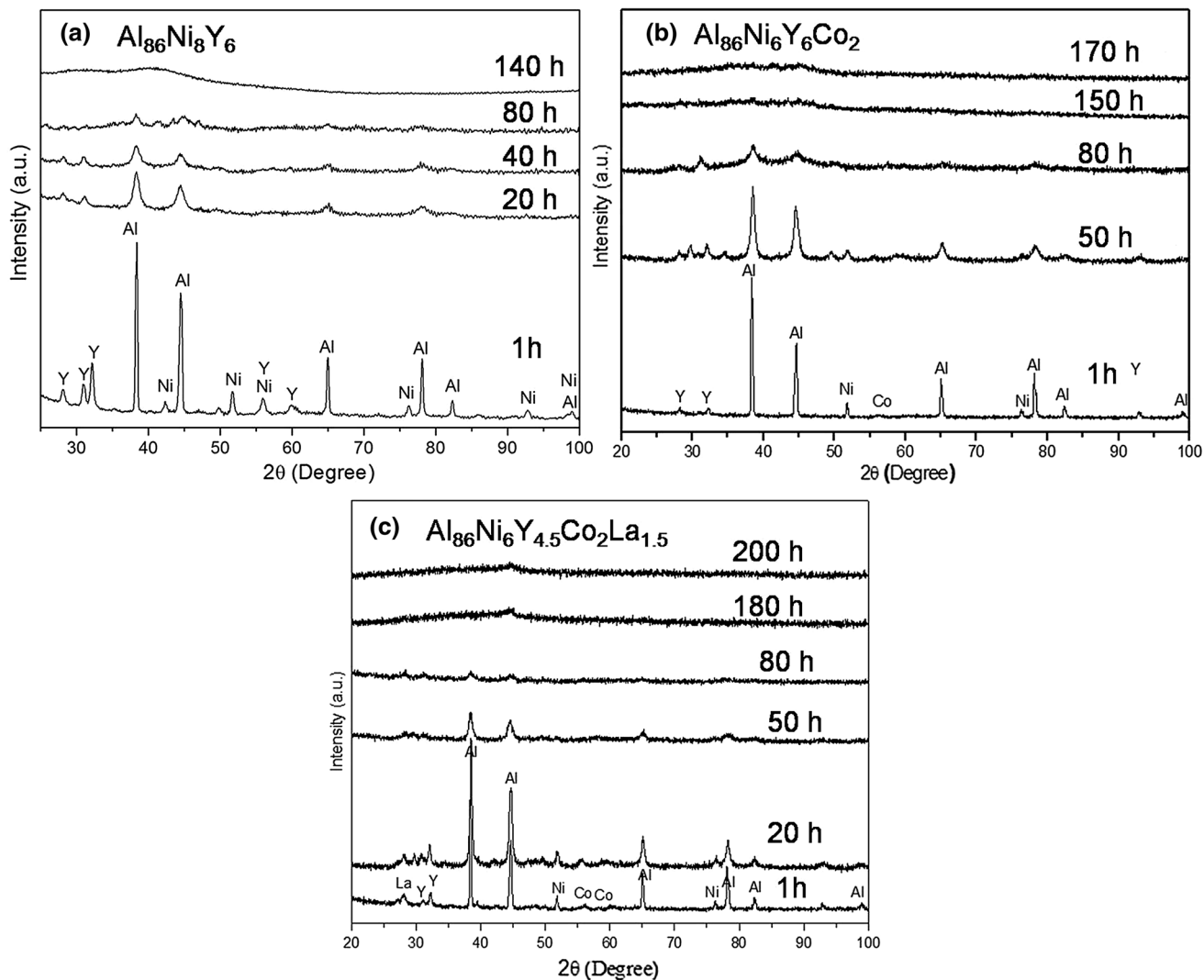
Fig. 1 XRD patterns of different interval milled (a) $Al_{86}Ni_8Y_6$, (b) $Al_{86}Ni_6Y_6Co_2$ and (c) $Al_{86}Ni_6Y_{4.5}Co_2La_{1.5}$ powder mixtures showing microstructural phase evolution with progress in milling time

earth elements La (1.885 Å) and Y (1.831 Å), attributed to the fact that atomic size differences of transition metals with the solvent element Al are well within the 15% range. Slightly delayed dissolution of Co in comparison with Ni (in $Al_{86}Ni_6Y_6Co_2$) and La in comparison with Y (in $Al_{86}Ni_6Y_{4.5}Co_2La_{1.5}$) is attributed to the higher atomic radius of earlier elements, respectively, which ultimately delayed the amorphization of $Al_{86}Ni_6Y_6Co_2$ and $Al_{86}Ni_6Y_{4.5}Co_2La_{1.5}$ powders. The mechanism of deformation during mechanical alloying for the various alloy powders was similar; however, the stages of phase transformation varied depending on the number and type (radii) of elements present in the alloy powders as confirmed by the corresponding XRD patterns shown in Fig. 1.

It should be mentioned here that during the course of milling, formation of metastable Al-rich complex phases was reported in the alloy powders as confirmed by the evolution of new peaks in the XRD patterns (Fig. 1). For example, the XRD pattern of the 80-h milled $Al_{86}Ni_8Y_6$ powders showed appearance of multiple peaks (between 40° and 50°) related to Al-rich intermetallic phases other than the primary elemental (Al, Ni,

Y) peaks as shown in Fig. 1(a). Similar XRD peak evolution was also observed in the 50-h milled $Al_{86}Ni_6Y_6Co_2$ alloy powders in the 2θ range of 25°-35° (Fig. 1b), exhibiting the formation of Al-rich complex phases. In the case of the quinary alloy powders ($Al_{86}Y_6Ni_{4.5}Co_2La_{1.5}$), the evolution of new peaks was observed in 20-h milled powders in the same 2θ range (25°-35°, Fig. 1c), indicating the formation of new phases. The formation of Al-rich intermetallic phases is attributed to the solid-state diffusion reaction based on the Hume-Rothery rule of dissolution (Ref 25-28). Earlier, Povstugar et al. (Ref 29) also reported formation of such intermetallic phases in the 50-h and 100-h milled $Al_{85}Y_8Ni_5Co_2$ powder. This Al-rich phase may form at any stages of milling; however, in this work, we report only a few interval milled powders as it would be tedious to analyze the instantaneous phase formation during milling. Also, Al-rich system requires prolonged amorphization time, which was attributed to the soft and ductile nature of aluminum with high stacking fault energy (Ref 8, 9, 30). $Al_{86}Ni_8Y_6$, $Al_{86}Ni_6Y_6Co_2$ and $Al_{86}Ni_6Y_{4.5}Co_2$ $La_{1.5}$ alloy powders milled up to 140, 170 and 200 h,
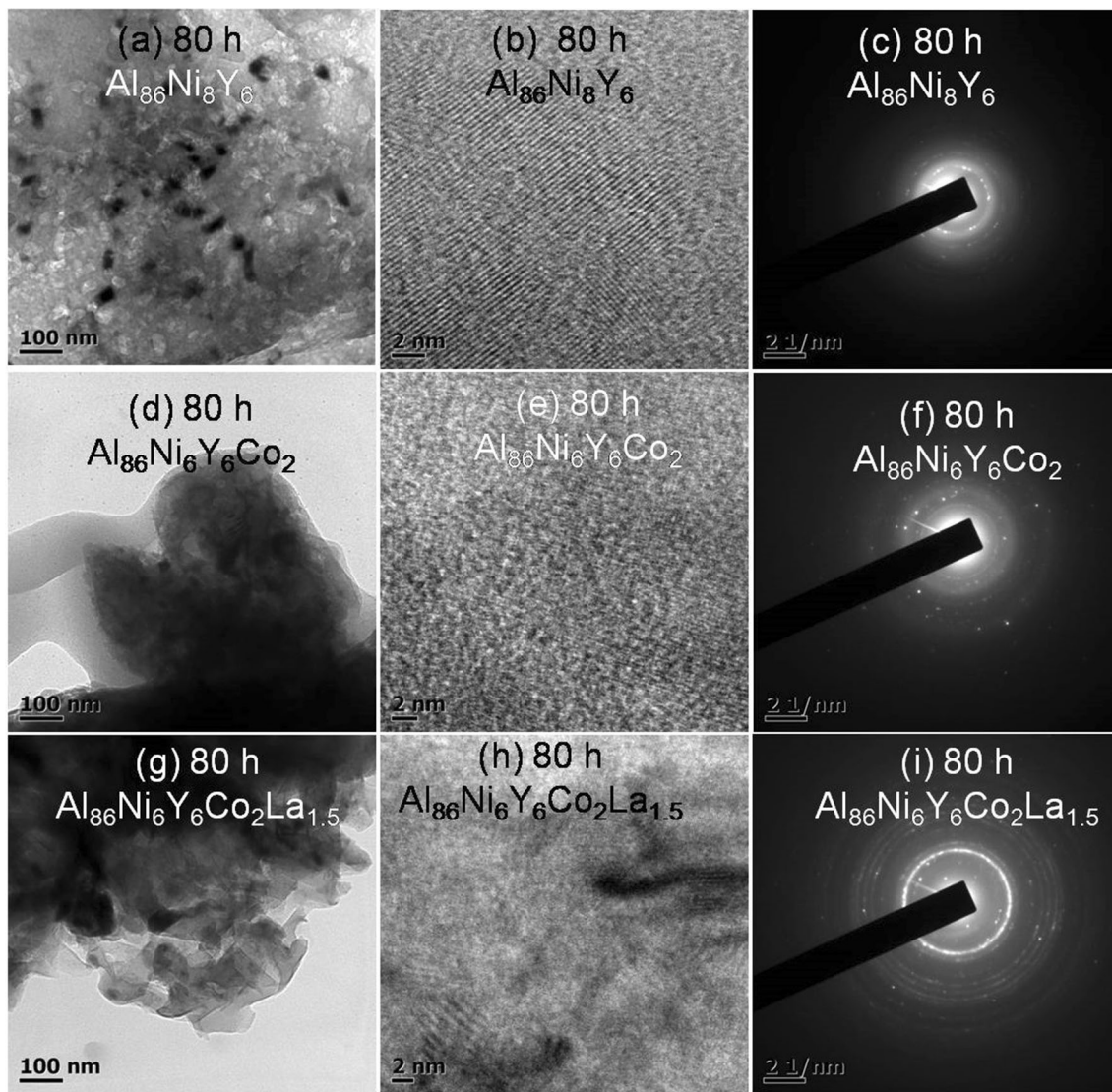
Fig. 2 TEM images and corresponding SAD patterns of the 80-h milled multicomponent powders showing the presence of amorphous and crystalline phases

respectively, exhibited broad XRD patterns without any detectable traces of crystalline peaks, confirming nearly full amorphization as shown in Fig. 1(a), (b) and (c), respectively.

3.1.2 Comparative Phase Analysis Based on TEM Results. Figure 2 displays the TEM images and SAD patterns of the three different composition powders milled for 80 h. The $Al_{86}Ni_8Y_6$ powder milled for 80 h exhibited various nanocrystalline Al-rich phases together with amorphous traces as shown in Fig. 2(a) and (b). This result was in accordance with the corresponding XRD pattern (Fig. 1a) shown earlier, which exhibited multiple peak presence in the 2θ range of 35°-45°. The corresponding high-resolution TEM image (Fig. 2b) clearly depicts the crystalline–amorphous patches. The related SAD pattern (Fig. 2c) showing diffused background with bright dots and discrete ring pattern also confirms the presence of the amorphous and nanocrystalline phase mixture.

Microstructural deformation was reported to be similar to $Al_{86}Ni_6Y_{4.5}Co_2$ and $Al_{86}Ni_6Y_{4.5}Co_2La_{1.5}$ powders as evidenced by respective TEM micrographs shown in Fig. 2(d)-(f) and (g)-(i) and XRD patterns (Fig. 1b and c), respectively. However, comparing the SAD patterns of the 80-h milled

$Al_{86}Ni_8Y_6$, $Al_{86}Ni_6Y_6Co_2$ and $Al_{86}Ni_6Y_{4.5}Co_2La_{1.5}$ powders (Fig. 2c, f and i), it could be envisaged that the ternary and quaternary systems exhibited more number of bright dots in comparison with the quinary system. On the other hand, the SAD pattern of the quinary milled powder consists of closely spaced rings with a lower number of bright dots. The presence of bright dots indicated the formation of Al-rich complex phases, whereas the rings indicate nanocrystallization. Thus, it could be deduced that $Al_{86}Ni_8Y_6$ and $Al_{86}Ni_6Y_6Co_2$ powders underwent an early phase transition in comparison with the $Al_{86}Ni_6Y_{4.5}Co_2La_{1.5}$ powder. The quinary alloy showed various ring patterns, indicating more degree of nanocrystallinity instead of Al-rich complex phase formation and thus extending the amorphization time to 200 h. Therefore, the glass-forming ability of the various multicomponent systems could also be qualitatively investigated by comparing the respective SAD patterns of the 80-h milled powders.

In a nutshell, the multicomponent alloy powders, viz. $Al_{86}Ni_8Y_6$, $Al_{86}Ni_6Y_6Co_2$ and $Al_{86}Ni_6Y_{4.5}Co_2La_{1.5}$, yielded fully amorphous phase after 140 h, 170 h and 200 h, respectively, confirmed by distorted lattice structure in high-resolution

TEM images and corresponding fully diffused SAD patterns. The TEM image and SAD pattern of the quinary ($Al_{86}Ni_6Y_{4.5}Co_2La_{1.5}$) amorphous powder are presented in Fig. 3.

3.2 Comparative Phase Analysis of the Consolidated Al-TM (Ni, Co)-RE (Y, La) Bulk Alloys

3.2.1 Phase Evolution in the 300 °C-Sintered Samples. XRD patterns of the 300 °C-sintered $Al_{86}Ni_8Y_6$, $Al_{86}Ni_6Y_6Co_2$ and $Al_{86}Ni_6Y_{4.5}Co_2La_{1.5}$ samples are shown in Fig. 4. XRD pattern of the ternary system ($Al_{86}Ni_8Y_6$) is fully broad without any detectable crystalline peaks, whereas the quaternary and quinary compositions exhibited a low-intensity nanocrystalline FCC-Al peak overlaying on broad amorphous hump. Thus, the lower-temperature-sintered samples retained a large amount of amorphous phase without major devitrification except the formation of a few amount of FCC-Al; however, compositions with a higher number of components tend to devitrify faster.

TEM study conducted on the 300 °C-sintered samples is reported in Fig. 5. TEM image of $Al_{86}Ni_8Y_6$ (Fig. 5a) exhibited nanocrystalline FCC-Al phase, which was not detected by XRD analysis (Fig. 4), and it may be due to negligible amount. The related SAD pattern (Fig. 5b) is fully diffused indicating retention of completely amorphous phase. The corresponding high-resolution image (Fig. 5c) exhibits no traces of lattice periodicity confirming the retention of amorphous phase. A similar analysis was performed for the quaternary and quinary compositions, and the corresponding TEM images (Fig. 5d and g) show the distribution of very few nanocrystalline FCC-Al in

the amorphous phase. However, comparing the SAD patterns of the quaternary and quinary systems, it was observed that former one shows a nearly diffused pattern without any bright dots, whereas the latter one exhibits a diffused pattern with some bright dots. This indicates that the composition containing a higher number of components tends to devitrify faster. HRTEM images of $Al_{86}Ni_6Y_6Co_2$ and $Al_{86}Ni_6Y_{4.5}Co_2La_{1.5}$ bulk sam-
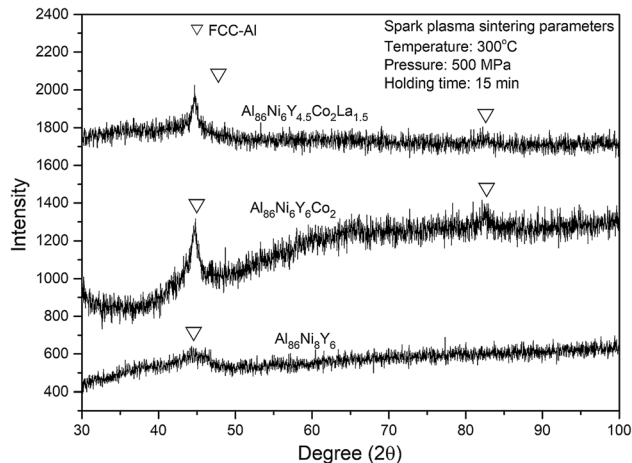

Fig. 4 XRD patterns of the 300 °C-sintered bulk samples showing amorphous hump overlaid by FCC-Al nanocrystalline peaks
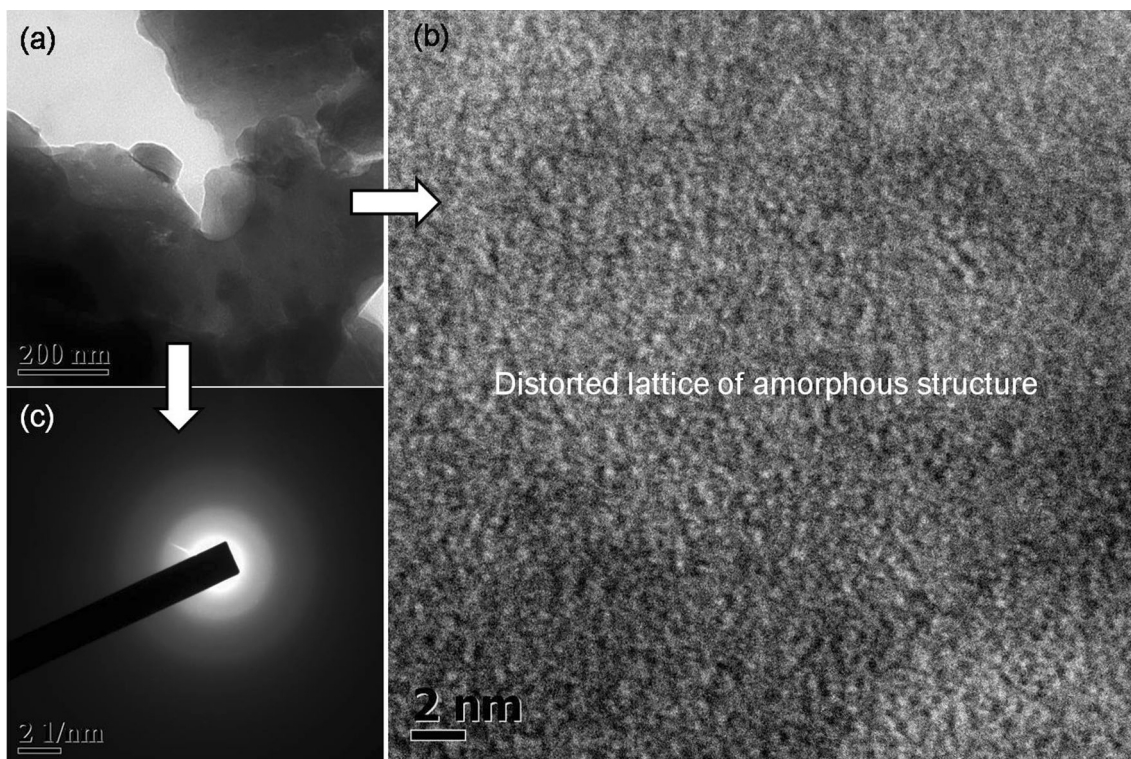

Fig. 3 (a) Featureless TEM image, (b) HRTEM image showing the distorted lattice structure related to amorphous phase and corresponding (c) diffused SAD patterns showing full amorphization in 170-h mechanically alloyed quinary $Al_{86}Ni_6Y_{4.5}Co_2La_{1.5}$ powders
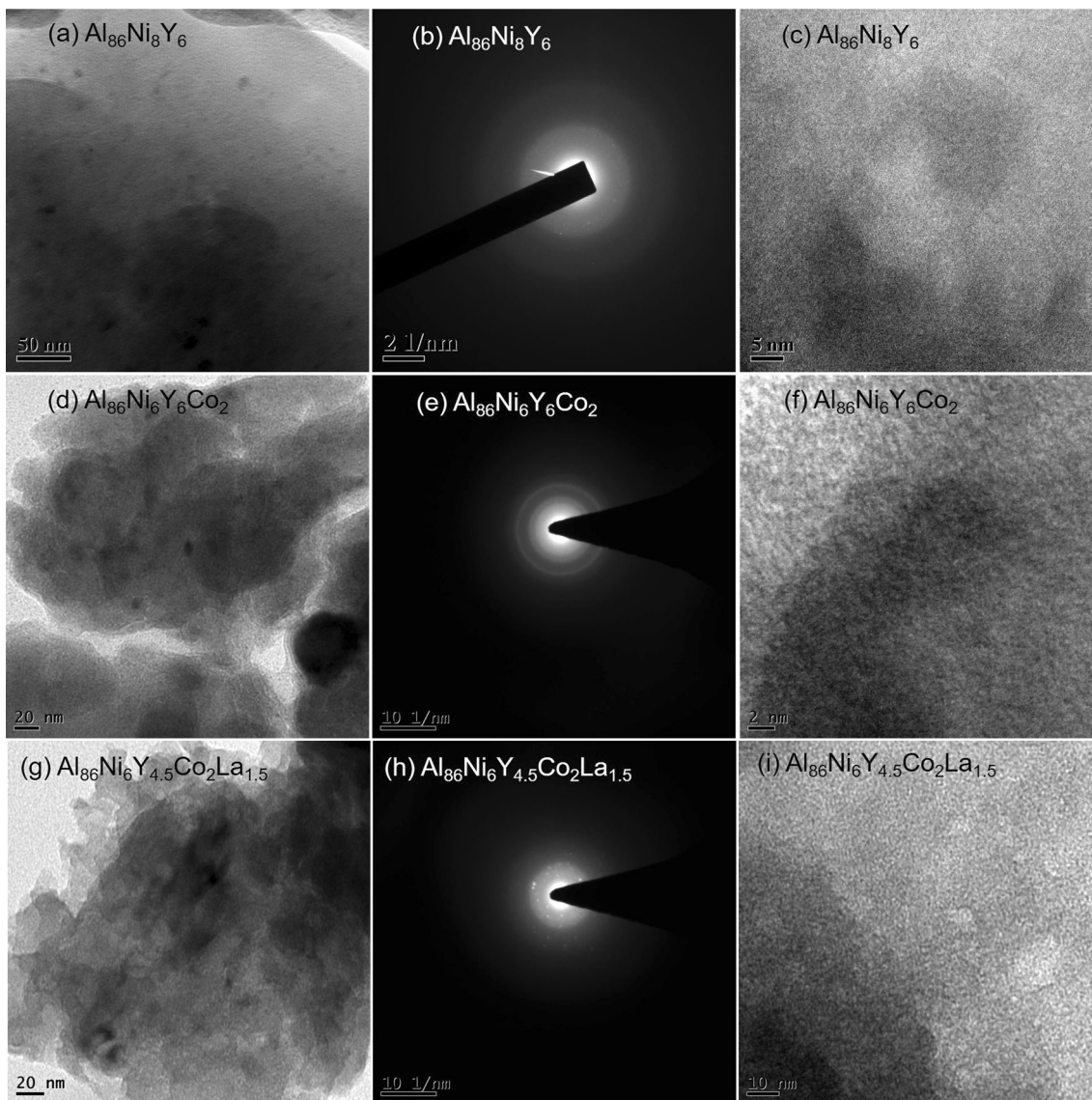
Fig. 5 TEM images, SAD patterns and corresponding HRTEM images of the various multicomponent bulk samples consolidated at 300 °C, showing amorphous matrix with a very few nanocrystalline FCC-Al phases

ples also revealed no traces of periodic lattice as shown in Fig. 5(f) and (i), respectively.

3.2.2 Phase Evolution in the 500 °C-Sintered Samples. The XRD patterns, differentiating the devitrification behavior of the 500 °C-sintered ternary, quaternary and quinary compositions, are shown in Fig. 6.

The XRD pattern of $Al_{86}Ni_8Y_6$ shows broad and deep hump overlaid by sharp FCC-Al crystalline peaks along with the appearance of some other peaks, evincing retention of good amount of amorphous phase along with the precipitation of various intermetallic phases. In the case of $Al_{86}Ni_6Y_6Co_2$, the retention of XRD hump (Fig. 6) significantly reduced and evolution of multiple peaks was observed, indicating retention of a lower fraction of amorphous phase. When the number of components was increased to five (viz. $Al_{86}Ni_6Y_{4.5}Co_2La_{1.5}$), the tendency of devitrification drastically increased as confirmed by the diminished XRD hump and emergence of various sharp peaks of intermetallic phases.

The devitrification tendency study of the 500 °C-sintered compositions was extended by TEM analysis as shown in Fig. 7. The TEM images (Fig. 7a, d and g) clearly show an increase in the number density of nanocrystalline precipitates with the increase in the number of components. The corresponding SAD pattern of ternary (Fig. 7b), quaternary (Fig. 7e) and quinary (Fig. 7h) systems clearly shows an increase in bright dots indicating more amount of phase formation and thus higher devitrification tendency. The corresponding XRD patterns (Fig. 6) were also consistent with these TEM images (Fig. 7). High-resolution TEM images of the 500 °C-sintered $Al_{86}Ni_8Y_6$, $Al_{86}Ni_6Y_6Co_2$ and $Al_{86}Ni_6Y_{4.5}Co_2La_{1.5}$ alloys are shown in Fig. 7(c), (f) and (i), respectively, which exhibit nanocrystalline precipitate in the amorphous matrix. The different nanocrystalline intermetallic phases detected in various alloys were reported to be Al_4Ni_3, $Al_{0.9}Ni_{1.1}$, Al_3Y, Al_2Y, AlY, Al_3Ni, Al_3Ni_2, $Al_{13}Co_4$, Al_5Co_2 and $Al_{11}La_3$ along with nanocrystalline FCC-Al phase. The literature survey indicated
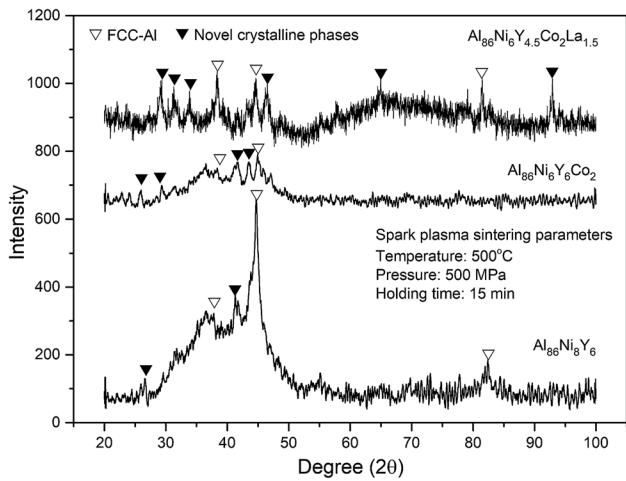
Fig. 6 XRD patterns of the 500 °C-sintered various aluminum-rich bulk alloys showing an enhanced devitrification tendency with the increase in the number of components in the alloy

evolution of multiple peaks overlaying on amorphous hump in the XRD pattern of the 500 °C spark plasma-sintered $Al_{88}Ni_6Ti_6$ glassy alloys (Ref 24). Similarly, Deng et al. (Ref 12) showed the presence of multiple XRD peaks without retention of XRD hump in the quinary spark plasma-sintered AlNiYCoLa alloy. The present authors have also studied the various temperature-consolidated $Al_{86}Ni_8Y_6$ and $Al_{86}Ni_6Y_6Co_2$ glassy alloys and found that an increase in sintering temperature assisted in faster devitrification phenomena (Ref 10).

3.3 Mechanism of Devitrification in Sintered Al-TM (Ni, Co)-RE (Y, La) Bulk Alloys

Mechanism of devitrification during sintering of metallic amorphous powders is still ambiguous and speculative to some extent (Ref 31, 32). There are various factors/parameters, which influence the sintering kinetics/behavior of amorphous powders such as (1) sintering parameters (viz. pressure, temperature and time), (2) constituents/chemical composition of amorphous powders, (3) synthesis methods (viz. milling, gas atomization, etc.) and (4) consolidation techniques (viz. hot pressing, spark plasma sintering, conventional sintering, etc.).

3.3.1 Role of Sintering Temperature. Sintering temperature influences the viscous nature and short-range periodicity of amorphous structure. Thus, the sintering mechanism of amorphous powders at various temperatures can be described by Stokes–Einstein equation (Ref 32). Atoms cluster in amorphous materials posses high viscosity and low mobility at lower sintering temperature (ideally $< T_g$) due to availability of low activation energy. The diffusivity of smaller radius atoms (viz. r_{Al}: 1.432 Å, r_{Ni}: 1.246 Å, r_{Co}: 1.253 Å) would be higher than larger-sized atoms (viz. r_Y: 1.831 Å, r_{La}: 1.885 Å), and this would result in decoupling of different atomic radii elements. Thus, Stokes–Einstein equation becomes irrelevant in case of low-temperature sintering, leading to a decrease in tendency of devitrification. This could be the reason behind the retention of large amount of amorphous phase in the 300 °C-sintered samples as confirmed by the XRD (Fig. 4) and TEM analysis (Fig. 5). Briefly, the XRD patterns of the 300 °C-sintered samples shown in Fig. 4 showed retention of amorphous phase along with a very less amount of FCC-Al

formation. The corresponding TEM images also showed no traces of crystalline phases except the formation of minor amount of nanocrystalline FCC-Al phase as shown in Fig. 5. On the other hand, at comparatively higher sintering temperature, coupling of larger and smaller atomic radii elements dominated due to the decrease in viscosity and faster diffusion kinetics following Stokes–Einstein equation (Ref 32), promoting the formation of a various *Al-TM-*, *Al-RE-*, *TM-RE-* and *Al-TM-RE-*based intermetallic phases. In the present study, the formation of various intermetallic phases in the 500 °C-sintered samples was confirmed from the emergence of the various peaks in the XRD patterns (Fig. 6) other than that of FCC-Al peaks as discussed earlier.

3.3.2 Role of Sintering Pressure. Literature survey points out that sintering pressure could contribute toward major change in atom spacing, chemical bonding and Gibbs free energy of phase transformation which collectively plays a decisive role in governing nucleation and growth during devitrification of glassy alloys (Ref 33-35). The highly viscous nature of amorphous powders limits the diffusion flowability of atoms (Ref 36, 37); however, the increasing temperature and pressure could effectively result in better atomic flow by reducing the viscosity. Jin et al. (Ref 38) reported that pressure influences structural relaxation which controls the densification and devitrification mechanism in metallic glasses. The structural relaxation at elevated temperature and pressure involves stress relaxation, atomic movement and shuffling, and annihilation of excess free volume. High sintering pressure assists in shear fracturing and fragmentation of brittle amorphous particles and thus collapses the free inter-particle space. Also, the absence of long-range diffusion, especially at high pressure and low temperature, could suppress the growth of crystallite nuclei, and thus, the alloy may retain higher amounts of the amorphous phase. Moreover, deformation caused by high pressure can promote short-range atomic rearrangement in metallic glasses by a reduction in the free volume (Ref 21). This small amount of reduction in free volume itself can promote a short-range ordering of atoms (Ref 33, 39), which increases atomic mobility and diffusion process to a certain extent, leading to the formation of only nanocrystalline phases. The formation of nanocrystalline phases in Al-La-Ni amorphous alloy subjected to very high pressure (1 Gpa) has been reported by Ye et al. (Ref 33). Li et al. (Ref 23) reported the formation of nanometric Al_5Co_2 during high-pressure sintering of $Al_{86}Ni_6Y_{4.5}Co_2La_{1.5}$ metallic glass powder attributed to abnormal crystallization. In the present work, formation of various nanocrystalline phases has been reported in various Al-based bulk alloys sintered at a temperature and pressure of 500 °C and 500 MPa for 15 min. However, alloys showed the difference in the amount of nanocrystalline phase precipitation depending on the number of component present in the alloy system.

3.4 Role of Particle Morphology

Other than temperature and pressure, particles morphology (viz. shape, size, structure) also plays a decisive role in dictating the sintering mechanism and influences the phase evolution and densification process (Ref 21, 22, 40). Nowak et al. (Ref 22) reported that glassy structures produced from sintering of smaller-sized amorphous powder particles, exhibited higher compressive strength in comparison with that
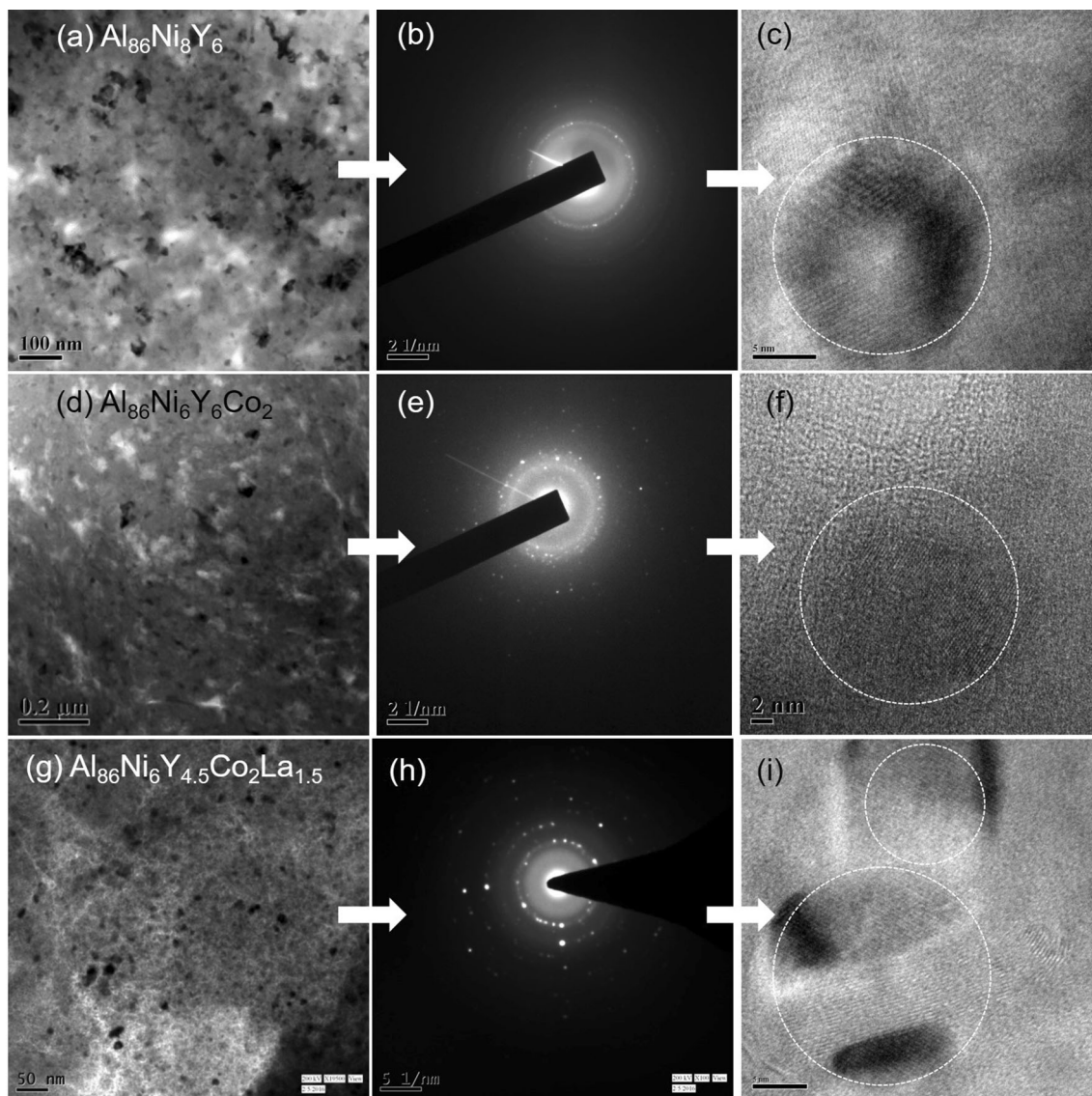
Fig. 7 (a, d, g) TEM images, corresponding (b, e, h) SAD patterns and corresponding (c, f, i) HRTEM images of $Al_{86}Ni_8Y_6$, $Al_{86}Ni_6Y_6Co_2$ and $Al_{86}Ni_6Y_{4.5}Co_2La_{1.5}$ bulk alloys, respectively, showing an increase in the number density of nanocrystalline phase evolution in amorphous matrix with the increase in the number of components in the alloy system

produced from larger-sized amorphous powders of similar composition. During spark plasma sintering, particles size variation and contact morphology are considered to be the primary reason behind electric discharge spatial distribution, uneven current density and localized heat distribution (Ref 21, 40). Apart from particles morphology, the factors which lead to uneven heat distribution during sintering are (1) spaces between contacting particles, (2) particles' contact surface area, (3) nature of particles and (4) ratio of permittivity of particles and air present in the inter-particle spaces (Ref 22, 23, 39, 41).

Further understanding of the effect of particles contact morphology on phase precipitation in the 500 °C-sintered $Al_{86}Ni_6Y_{4.5}Co_2La_{1.5}$ alloy could be obtained from the TEM images shown in Fig. 8. Rich and deficit region of crystalline phases is clearly shown in Fig. 8. The SAD patterns from the crystalline-rich area consist of many bright dots (Fig. 8b), whereas SAD pattern from amorphous-phase-rich portion looks more diffused with fewer bright dots (Fig. 8c). The reason behind the difference in phase variation could be attributed to the change in particles' contact surface area in the milled powders. Crystalline-phase-rich areas are expected to be the connecting boundary for at least two particles where the current density was high leading to temperature shooting up followed by various phase precipitation (Fig. 8a).

3.4.1 Role of Chemical Composition. Another important factor, which greatly influences the sintering behavior of metallic amorphous powders, is their chemical compositions (Ref 4, 12, 13, 24, 32, 34). The interesting outcome of the present work is that a higher number of components in the Al-TM-RE alloy system supplemented the devitrification phenomena as confirmed from the comparative study of XRD patterns of the 500 °C-sintered $Al_{86}Ni_8Y_6$, $Al_{86}Ni_6Y_6Co_2$ and $Al_{86}Ni_6Y_{4.5}Co_2La_{1.5}$ shown earlier in Fig. 6. The XRD pattern of

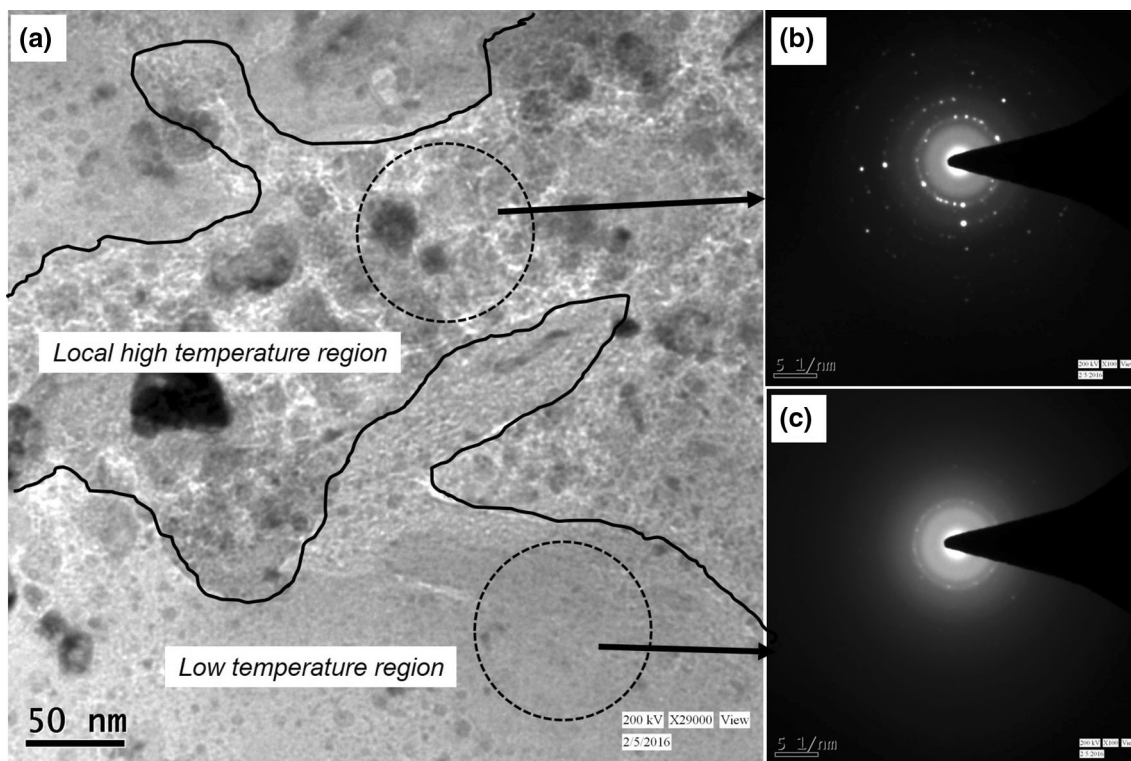**Fig. 8** $Al_{86}Ni_6Y_{4.5}Co_2La_{1.5}$ sintered at 500 °C: (a) TEM image showing rich and deficit region of precipitates, (b) SAD pattern from precipitate-rich region showing bright dots and (c) SAD pattern from amorphous rich area showing diffused pattern with fewer dots

Table 1 Enthalpy of mixing of the aluminum-based ternary, quaternary and quinary multicomponent systems

Multicomponent alloy system	Enthalpy of mixing, kJ/mol	Configurational entropy, J/K mol
$Al_{86}Ni_8Y_6$	− 14.5	4.162
$Al_{86}Ni_6Y_6Co_2$	− 14.2	4.536
$Al_{86}Ni_6Y_{4.5}Co_2La_{1.5}$	− 14.2	4.816

quinary $Al_{86}Ni_6Y_{4.5}Co_2La_{1.5}$ exhibited multiple peaks without retention of the amorphous hump, whereas the hump was more pronounced in the ternary $Al_{86}Ni_8Y_6$ bulk alloy. Other than the temperature, a higher number of components also assist in increasing configurational entropy, which enhances the probability of atom coupling following Stokes–Einstein equation leading to more crystallization as explained in the above section. The configuration entropy was estimated for the different compositions using the following equation:

$$S_{\text{Configuration}} = k \ln \Omega = -R(X_A \ln X_A + X_B \ln X_B + \cdots)$$
(Eq 1)

The calculated values of the configurational entropy for different compositions are presented in Table 1. It should be mentioned here that the above equation is valid for periodic arrangement of atoms as in crystalline structure; however, amorphous structure possesses higher enthalpy, entropy and free energy than the crystalline counterpart. Atomic arrangement in Al-TM-RE metallic glass system has been proposed by Miracle et al. (Ref 5) and Ma et al. (Ref 7). A schematic of the packing mode in Al-TM-RE systems is shown in Fig. 9, in which the RE and TM solute-centered clusters are connected

through Al atoms (Ref 7). As per this method, the optimum composition of glass formation should allow each Al atom to be shared simultaneously by a TM-centered cluster and a RE-centered cluster that is the most efficiently packed. Thus, all the Al atoms are energetically stabilized and all clusters are efficiently packed and connected. In the presence of sufficient driving force, the structural relaxation and free volume annihilation take place leading to short-range atomic arrangement and thus formation of nanocrystalline intermetallic phases (Ref 9). Higher configurational entropy of quinary system increased the chance of coupling of atoms as the probability of finding the different neighboring element increased, whereas the lower configurational entropy of ternary system facilitated lower probability of coupling among atoms as per Stokes–Einstein equation.

3.5 Relative Density and Hardness of Consolidated Bulk Alloys

Relative density and hardness of the sintered glassy samples of varying compositions are graphically represented in Fig. 10. The small differences in relative density of the samples sintered with similar sintering parameters could be explained on the
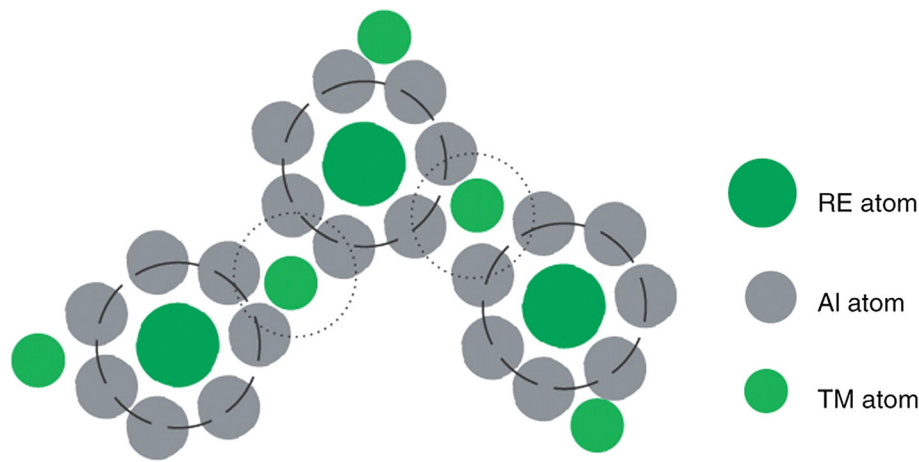
Fig. 9 Schematics of the efficient cluster packing (ECP) in Al-TM-RE metallic glasses (Ref 7)
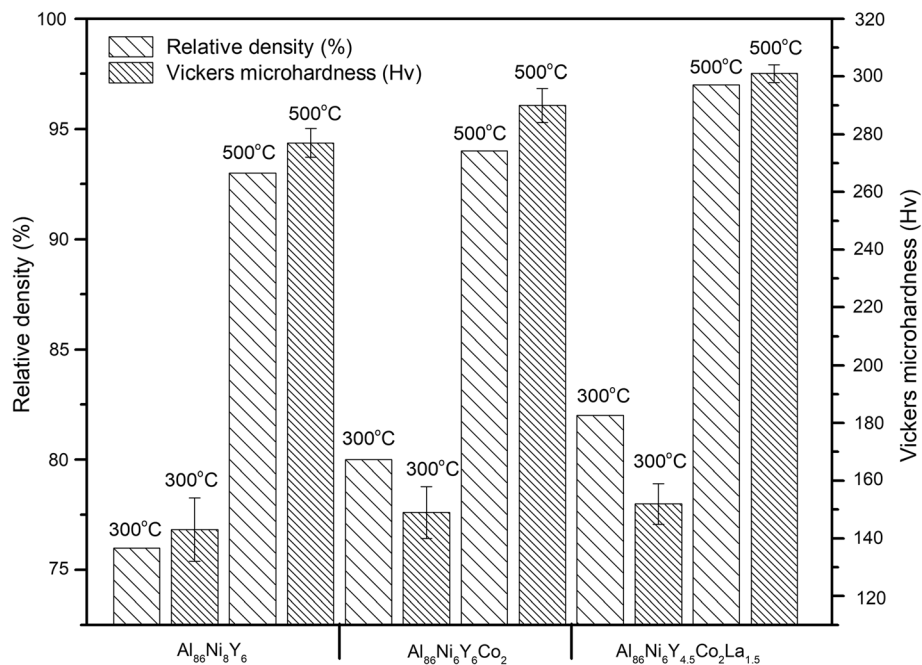

Fig. 10 Relative density and microhardness of different Al-based consolidated bulk alloys at different temperatures

basis of differences in the degree of structural relaxation and crystallization. High-pressure deformation and an increase in sintering temperature promote structural relaxation, i.e., diffusion annihilation of free volume, leading to short-range atomic arrangement (Ref 21, 39, 41, 42). Thus, the annihilation of free volume impacts the relative density of the sintered sample. Precise measurement of annihilated free volume is very difficult; however, the difference in relative density could give an idea about the free volume annihilation. Degree of crystallization also affects the relative density as crystallization involves atomic rearrangement during which free volume gets annihilated. Thus, the sintered alloys which exhibited a faster tendency of crystallization yielded higher relative density. In this context, the 300 °C-sintered $Al_{86}Ni_6Y_{4.5}Co_2La_{1.5}$ and $Al_{86}Ni_6Y_6Co_2$ (quaternary and quinary) samples yielded higher relative density (73%) in comparison with the ternary $Al_{86}Ni_8Y_6$ (71%), sintered in similar conditions. The crystal-

lization tendency of the 300 °C-sintered alloys was reported to be nearly similar; however, the close observation revealed that a five-component system showed a higher tendency of crystallization. A similar trend was observed while comparing the relative density of the 500 °C-sintered samples. The quinary alloy system exhibited higher relative density of 94%, whereas lower density was reported in the case of the 500 °C-sintered $Al_{86}Ni_6Y_6Co_2$ alloys (92%) due to retention of the amorphous hump as amorphous phase contains free volumes. The 500 °C-sintered $Al_{86}Ni_8Y_6$ alloy yielded even lower relative density (91%) attributed to the larger amount of retained amorphous phase as confirmed by the considerable hump in the XRD pattern (Fig. 6).

Hardness of various consolidated bulk alloys was also reported to be in the similar range. Ternary $Al_{86}Ni_8Y_6$ bulk alloy exhibited hardness of 277 Hv due to retention of larger amounts of amorphous phase along with the distribution of

nanocrystalline phase. Quaternary $Al_{86}Ni_6Y_6Co_2$ bulk alloy exhibited higher hardness of 290 Hv attributed to the more amount of nanocrystalline phase distributed in amorphous matrix as confirmed by the reduced hump in the XRD pattern (Fig. 6). However, the hardness of quinary $Al_{86}Ni_6Y_{4.5}Co_2La_{1.5}$ bulk alloy (301 Hv) was comparatively higher than that of the ternary and quaternary bulk alloys which could be attributed to the formation of large amounts of nanocrystalline phase at the expense of amorphous phase as confirmed by the evolution of multiple peaks in the XRD pattern (Fig. 6). Similar trends in hardness of $Zr_{60}Cu_{10}Al_{15}Ni_{15}$ alloy were reported by Vincent et al. (Ref 40). They reported the highest hardness in nearly fully crystalline $Zr_{60}Cu_{10}Al_{15}Ni_{15}$ alloy, whereas partially crystalline $Zr_{60}Cu_{10}Al_{15}Ni_{15}$ alloy exhibited lower hardness value; however, fully glassy $Zr_{60}Cu_{10}Al_{15}Ni_{15}$ alloy possesses least hardness value.

4. Conclusions

Summarily, a comparative study of the amorphization tendency of mechanically alloyed $Al_{86}Ni_6Y_6$ (140 h), $Al_{86}Ni_6Y_6Co_2$ (170 h) and $Al_{86}Ni_6Y_{4.5}Co_2La_{1.5}$ (200 h) powders and consecutively the devitrification tendency of consolidated bulk alloys was performed. The requirement of prolonged milling time of amorphization was attributed to the soft and ductile nature of aluminum together high stacking fault energy. Various Al-based bulk alloys consolidated at 300 °C exhibited very few nanocrystalline FCC-Al distributed in amorphous matrix as confirmed by low-intensity FCC-Al peak overlaying broad XRD hump. More devitrification was reported in the 500 °C-sintered various alloys with a large variation in degree of devitrification of $Al_{86}Ni_8Y_6$, $Al_{86}Ni_6Y_6Co_2$ and $Al_{86}Ni_6Y_{4.5}Co_2La_{1.5}$ bulk alloys. Quinary $Al_{86}Ni_6Y_{4.5}Co_2La_{1.5}$ bulk alloy exhibited more devitrification attributed to the higher probability of coupling of atoms by short-range atomic shuffling. The devitrification tendency decreased with the decrease in number element in the alloy system as confirmed by the more pronounced hump in the XRD patterns of alloys containing lower solute elements. Reported various Al-rich phases in the 500 °C-sintered different alloys were Al_4Ni_3, $Al_{0.9}Ni_{1.1}$, AlY, Al_3Ni_2, $Al_{13}Co_4$, Al_5Co_2 and $Al_{11}La_3$ along with FCC-Al as revealed by detailed XRD and TEM study. Slight variation in relative density and hardness of different Al-based bulk alloys were attributed to the variation in degree of free volume annihilation and crystallization.

References

1. W.H. Wang, C. Dong, and C.H. Shek, Bulk Metallic Glasses, *Mater. Sci. Eng. R*, 2004, **44**, p 45–89
2. C.A. Schuh, T.C. Hufnagel, and U. Ramamurty, Mechanical Behavior of Amorphous Alloys, *Acta Mater.*, 2007, **55**, p 4067–4109
3. B.J. Yang, J.H. Yao, J. Zhang, H.W. Yang, J.Q. Wang, and E. Ma, Al-Rich Bulk Metallic Glasses with Plasticity and Ultrahigh Specific Strength, *Scripta Mater.*, 2009, **61**, p 423–426
4. X.P. Li, M. Yan, H. Imai, K. Kondoh, J.Q. Wang, G.B. Schaffer, and M. Qian, Fabrication of 10 mm Diameter Fully Dense $Al_{86}Ni_6Y_{4.5}Co_2La_{1.5}$ Bulk Metallic Glass with High Fracture Strength, *Mater. Sci. Eng. A*, 2013, **568**, p 155–159
5. D.B. Miracle, The Efficient Cluster Packing Model—An Atomic Structural Model for Metallic Glasses, *Acta Mater.*, 2006, **54**, p 4317–4336
6. H.W. Sheng, Y.Q. Cheng, P.L. Lee, S.D. Shastri, and E. Ma, Atomic Packing in Multicomponent Aluminium-Based Metallic Glasses, *Acta Mater.*, 2008, **56**, p 6264–6272
7. C.S. Ma, J. Zhang, W.L. Hou, X.C. Chang, and J.Q. Wang, Efficient Atomic Packing Clusters and Glass Formation In Ternary Al-Based Metallic Glasses, *Philos. Mag. Lett.*, 2008, **88**, p 599–605
8. R.S. Maurya and T. Laha, Effect of Rare Earth and Transition Metal Elements on the Glass Forming Ability of Mechanical Alloyed Al-TM-RE Based Amorphous Alloys, *J. Mater. Sci. Technol.*, 2015, **31**, p 1118–1124
9. R.S. Maurya, A. Sahu, and T. Laha, Effect of Consolidation Pressure on Phase Evolution During Sintering of Mechanically Alloyed $Al_{86}Ni_8Y_6$ Amorphous Powders Via Spark Plasma Sintering, *Mater. Sci. Eng. A*, 2016, **649**, p 48–56
10. R.S. Maurya, A. Sahu, and T. Laha, Quantitative Phase Analysis in $Al_{86}Ni_8Y_6$ Bulk Glassy Alloy Synthesized by Consolidating Mechanical Alloyed Amorphous Powder Via Spark Plasma Sintering, *Mater Des.*, 2016, **93**, p 96–103
11. R.S. Maurya, A. Sahu, and T. Laha, Microstructural and Phase Analysis of Al Based Bulk Metallic Glass Synthesized by Mechanically Alloying and Consecutive Spark Plasma Sintering with Varying Consolidation Pressure, *Adv. Mater. Lett.*, 2016, **7**, p 187–191
12. S.S. Deng, D.J. Wanga, Q. Luo, Y.J. Huang, and J. Shen, Spark Plasma Sintering of Gas Atomized AlNiYLaCo Amorphous Powders, *Adv. Powder Technol.*, 2015, **26**, p 1696–1701
13. T.T. Sasaki, K. Hono, J. Vierke, M. Wollgarten, and J. Banhart, Bulk Nanocrystalline $Al_{85}Ni_{10}La_5$ Alloy Fabricated by Spark Plasma Sintering of Atomized Amorphous Powders, *Mater. Sci. Eng. A*, 2008, **490**, p 343–350
14. C. Suryanarayana, *Mechanical Alloying and Milling*, Marcel Dekker Press, New York, 2004
15. Z. Huang, J. Li, Q. Rao, and Y. Zhou, Dependences of the Crystallization Behavior of Al-Ni-La Amorphous Alloys on La and Ni Contents, *J. Non Cryst. Solids*, 2008, **354**, p 1671–1677
16. Z.P. Chen, J.E. Gao, Y. Wu, H.X. Li, H. Wang, and Z.P. Lu, Role of Rare-Earth Elements in Glass Formation of Al-Ca-Ni Amorphous Alloys, *J. Alloys Compd.*, 2012, **513**, p 387–392
17. Z. Zhang, X.Z. Xiong, W. Zhou, X. Lin, A. Inoue, and J.F. Li, Glass Forming Ability and Crystallization Behavior of Al-Ni-RE Metallic Glasses, *Intermetallics*, 2013, **42**, p 23–31
18. Z. Zhang, X.Z. Xiong, W. Zhou, and J.F. Li, Influence of Substitution of La by Ce on the Glass Forming Ability and Crystallization Behavior of Al-Ni-La Alloys, *J. Alloys Compd.*, 2013, **576**, p 181–186

19. F. Guo, S. Enouf, G. Shiflet, and J. Poon, Role of Atomic Sizes on Glass Formability and Thermal Stability of Al-Based Amorphous Alloys, *Mater. Trans. JIM*, 2000, **41**, p 1406–1409

20. A.K. Gangopadhya and K.F. Kelton, Effect of Rare-Earth Atomic Radius on the Devitrification of $Al_{88}RE_8Ni_4$ Amorphous Alloys, *Philos. Mag.*, 2000, **8**, p 1193–1206

21. B. Zheng, D. Ashford, Y. Zhou, S.N. Mathaudhu, J. Delplanque, and E.J. Lavernia, Influence of Mechanically Milled Powder and High Pressure on Spark Plasma Sintering of Mg-Cu-Gd metallic glasses, *Acta Mater.*, 2013, **61**, p 4414–4428

22. X.J. Gu, J.Q. Wang, F. Ye, and K. Lu, Influence of Pressure on Crystallization Kinetics in an Al-Ni-Ce-Fe Amorphous Alloy, *J. Non cryst. Solids*, 2011, **296**, p 74–80

23. X.P. Li, M. Yan, G.B. Schaffer, and M. Qian, Abnormal Crystallization in $Al_{86}Ni_6Y_{4.5}Co_2La_{1.5}$ Metallic Glass Induced by Spark Plasma Sintering, *Intermetallics*, 2013, **39**, p 69–73

24. S. Mula, K. Mondal, S. Ghosh, and S.K. Pabi, Structure and Mechanical Properties of Al-Ni-Ti Amorphous Powder Consolidated by Pressure-Less, Pressure-Assisted and Spark Plasma Sintering, *Mater. Sci. Eng. A*, 2010, **527**, p 3757–3763

25. V. Raghavan, *Material Science and Engineering*, Prentice-Hall of India Private Limited Press, New Delhi, 1993

26. Z. Zhang, Y. Zhou, and E.J. Lavernia, Amorphization and Crystallization in Al-Ni-La During Mechanical Milling, *J. Alloys Compd.*, 2008, **466**, p 189–200

27. A.C. Lund and C.A. Schuh, Topological and Chemical Arrangement of Binary Alloys During Severe Deformation, *J. Appl. Phys.*, 2004, **95**, p 4815–4822

28. F. Delogu and G. Cocco, Numerical Simulations of Structural Modifications at a Ni-Zr Sliding Interface, *Phys. Rev. B*, 2005, **72**, p 014124

29. J.S. Kim, I.V. Povstugar, P.P. Choib, E.P. Yelsukovc, and Y.S. Kwona, Synthesis of Al-Y-Ni-Co Composites by Mechanical Alloying and Consecutive Spark-Plasma Sintering, *J. Alloy. Compd.*, 2009, **486**, p 511–514

30. I. Borner and J. Eckert, Phase Formation and Properties of Mechanically Alloyed Amorphous $Al_{85}Y_8Ni_5Co_2$, *Scripta Mater.*, 2001, **45**, p 237–244

31. P.G. Debenedetti and F.H. Stillinger, Supercooled Liquids and the Glass Transition, *Nature*, 2001, **410**, p 259–267

32. H.B. Yu, K. Samwer, Y. Wu, and W.H. Wang, Correlation Between β Relaxation and Self-Diffusion of the Smallest Constituting Atoms in Metallic Glasses, *Phys. Rev. Lett.*, 2012, **109**, p 095508

33. F. Ye and K. Lu, Pressure Effect on Crystallization Kinetics of an Al–La–Ni Amorphous Alloy, *Acta Mater.*, 1999, **47**, p 2449–2454

34. Z.Y. Shen, G.Y. Chen, Y. Zhang, and X.J. Yin, Pressure Effect on Superconducting Transition-Temperature Relaxation Behavior of the $Zr_{70}Cu_{30}$ Amorphous Alloy on Annealing at Elevated Pressures, *Phys. Rev. B*, 1989, **39**, p 2714

35. W.K. Wang, H. Iwasaki, C. Suryanarayana, and T. Masumoto, Crystallization Characteristics of an Amorphous $Ti_{80}Si_{20}$ Alloy at High Pressures, *J. Mater. Sci.*, 1983, **18**, p 3765–3772

36. H. Mehrer, *Diffusion in Solids*, Springer, Berlin, 2007

37. A. Zhu, G.J. Shiflet, and S.J. Poon, Diffusion in Metallic Glasses: Analysis from the Atomic Bond Defect Perspective, *Acta Mater.*, 2008, **56**, p 3550–3557

38. H.J. Jin, X.J. Gu, P. Wen, L.B. Wang, and K. Lu, Pressure Effect on the Structural Relaxation and Glass Transition in Metallic Glasses, *Acta Mater.*, 2003, **51**, p 6219–6231

39. K.S. Lee, J.H. Lee, and J. Eckert, On the Structural Relaxation of Bulk Metallic Glass Under Warm Deformation, *Intermetallics*, 2009, **17**, p 222–226

40. S. Vincent, B.S. Murty, M.J. Kramer, and J. Bhatt, Micro and Nano Indentation Studies on $Zr_{60}Cu_{10}Al_{15}Ni_{15}$ Bulk Metallic Glass, *Mater. Des.*, 2015, **65**, p 98–103

41. G. Yuan, K. Amiya, and A. Inoue, Structural Relaxation, Glass-Forming Ability and Mechanical Properties of Mg-Cu-Ni-Gd Alloys, *J. Non Cryst. Solid*, 2005, **351**, p 729–735

42. B.V. Aken, P.D. Hey, and J. Sietsma, Structural Relaxation and Plastic Flow in Amorphous $La_{50}Al_{25}Ni_{25}$, *Mater. Sci. Eng. A*, 2000, **278**, p 247–254